Design of a Wide Output Voltage Dual Active Bridge Converter as Power Electronics Building Block for the Fast Charging of Electric Vehicles

Al, Tim M. ; Lyu, Dingsihao; Soeiro, Thiago Batista; Bauer, Pavol

Important note
To cite this publication, please use the final published version (if applicable).
Please check the document version above.

Design of a Wide Output Voltage Dual Active Bridge Converter as Power Electronics Building Block for the Fast Charging of Electric Vehicles

Tim M. Al, Dingsihao Lyu, Thiago Batista Soeiro, and Pavol Bauer

Delft University of Technology (TU Delft)
DC Systems, Energy Conversion and Storage
Delft, The Netherlands
t.batistasoeiro@tudelft.nl

Abstract—This paper verifies the potential of utilizing the Dual Active Bridge (DAB) converter as a 10 kW Power Electronics Building Block (PEBB) for the charging of Electric Vehicles (EVs) where a wide output voltage range is required. Following the tendency of the new EV charging standards from CCS and CHAdeMO, the commonly employed isolated DC-DC converter should be able to supply the rated power for different vehicles which employ battery technologies which could range from 300 V up to 1000 V. Rectangular (or phase-shift), triangular and trapezoidal modulation strategies are investigated, of which the last two techniques are used for designing the PEBB. Suitable SiC-based semiconductors are chosen, the passive components are designed and the power losses are derived for the whole operating range. It is found that a high power efficiency can be achieved using the designed system.

Index Terms—Dual active bridge converter, DC-DC converter, Triangular, Trapezoidal, Current Modulation, Battery Charging, Electrical Vehicle

I. INTRODUCTION

With the increasing interest in reducing CO_2 emissions, the transport sector is gradually shifting towards Electrical Vehicles (EVs). This calls for large investments on public DC-type battery charging infrastructures which are efficient, fast and above all that can satisfy a plurality of vehicle technologies. Today most EVs can be charged at 50 kW and around 400 V following the DC-type fast charging standards CCS and CHAdeMO. However new EVs are designed to withstand much higher power, e.g. Porsche Mission-E, and due to the current limitation of the battery cells, higher battery bank voltages will become more often used [1]. To fulfill this demand new enhanced CCS and CHAdeMO standards have been developed which can withstand much higher power, e.g. 350 kW at up to 1 kV. Today, most EV batteries need to be charged with an initial voltage of around 300 V at low State-of-Charging (SoC) and an upper limit of up to about 800 V at high SoC [2]–[4].

Due to safety requirements multiport fast chargers commonly implement an isolated DC-DC converter technology in each port. Due to the buck and boost inherit capability and tight controllability of the Zero Voltage Switching (ZVS) operation the Dual Active Bridge (DAB) converter employing unipolar semiconductors, such as Silicon Carbide (SiC)

MOSFETs, seems an excellent circuit solution for a DC-DC converter of an EV charger with the requirement of a wide output voltage range. Additionally, the typical tight control of the current across the high frequency transformer also facilitates the parallel connection of several DABs. Hence, the DAB technology fits well for the concept of parallel circuit modularization for the output power scalability of the charger infrastructure by means of Power Electronics Building Blocks (PEBBs) [3], [4].. In this paper, a DAB will be designed rated to 10 kW to satisfy a plurality of EV charging applications. For example, this could be used as a PEBB for a fast 50 kW charging system. Further modularization could be used to increase the power capability as multiple of 50 kW, reaching 200 kW or 350 kW and above. The individual 10 kW module could also be used as a DC-type home charger. Finally, the converter module is specified to have an output voltage range from 300 V up to 1000 V. Note that the intrinsic bi-directionality of the DAB circuit could be also useful in the future in homes for Vehicle-to-Grid (V2G) power flow where the car battery is used as a storage buffer in the electricity grid. This functionality could be important to improve the distribution grid when considerable renewable energy sources are closely present [4]. This paper is divided as follows. Firstly, in Section II the DAB circuit operation will be discussed, followed by the derivation of the analytical model of the circuit operating with different modulation techniques in Section III. In Section IV, the 10 kW module is designed. Finally, in Section V the losses and resulting efficiency of the converter will be estimated.

II. DUAL ACTIVE BRIDGE CONVERTER

A circuit schematic of the DAB converter is given in Figure 1. The basic circuit consist of two full-bridge converters, with an inductor and high frequency transformer in between. The transformer provides the necessary isolation between both the EV and the grid, and among EVs for charging infrastructure where multiple cars can be simultaneously charged. The purpose of the inductor and the control of the semiconductors is to transfer the necessary power. In high frequency designs this inductor can be crafted to match the equivalent leakage

inductance of the transformer. The DAB is a bi-directional isolated DC-DC converter which incorporates buck and boost functionality. This is specially suited for maintaining high power conversion efficiency and voltage controllability for a wide variation of input and/or output voltages [5], [6], which are typical in battery charging applications. The implementation of unipolar semiconductors, such as SiC MOSFETs, is advantageous for reducing both conduction and switching losses when compared to Silicon (Si) bipolar technologies such as IGBTs and anti-parallel diodes. The ZVS turn-on capability of the DAB in combination to the intrinsic loss feature of the SiC device is particular interesting for achieving very low switching losses.
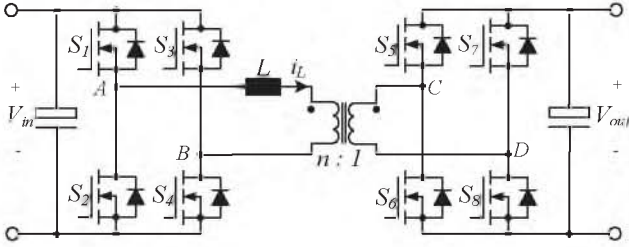

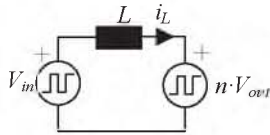Fig. 1: Circuit of the dual active bridge converter

Fig. 2: Equivalent operational circuit of the DAB converter

To simplify the analysis of the DAB converter, the equivalent circuit given in Figure 2 can be used. Herein, each full-bridge is represented by a controllable voltage source, where the secondary side voltage is reflected to the primary side considering the voltage gain imposed by the transformer turns ration. Based on the crafted voltage difference between the two voltage sources and the impedance of the inductor, a controllable current can flow from the charger to the EV, or vice-versa, as described by Equation (1).

$$i_L(t) = i_L(t_0) + \frac{1}{L} \int_{t_0}^{t_1} (v_{in} - n \cdot v_{out}) \cdot dt \quad (1)$$

III. DAB MODULATION SCHEMES

A. Rectangular Current Modulation

A widely used modulation scheme for the DAB is the single phase shift or rectangular current modulation [7]. The latter term will be used throughout this paper. Each inverter bridge operates in bipolar modulation, i.e. 50% duty cycle, with the primary side equivalent voltage source generating the voltage level of $+V_{in}$ or $-V_{in}$, while the secondary side voltage source creating the level of $n \cdot V_{out}$ or $-n \cdot V_{out}$. By forcing a phase shift angle ϕ between these equivalent voltage sources the amount of power to be transferred can be controlled.
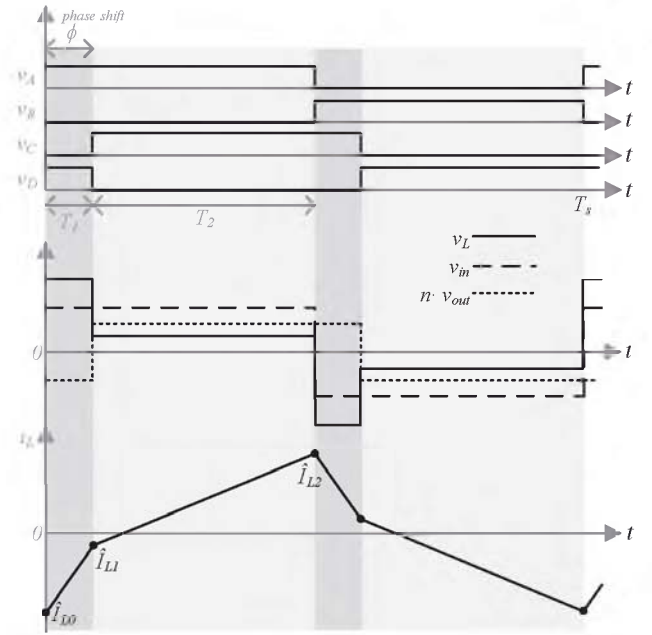

Fig. 3: Rectangular current modulation

To understanding the basic principle of the rectangular modulation one needs to take a close look to the voltage waveforms v_x generated by each half-bridge leg x ($x = A, B, C, D$) in Figure 3. When v_x is high, the top switch in leg x is triggered, otherwise the bottom switch is used. Using the resulting voltage waveforms of $v_A - v_B = v_{in}$ and $v_C - v_D = v_{out}$, the voltage across the inductor $v_L = v_{in} - n \cdot v_{out}$ can be obtained as well as the current i_L. The transferred power is then given by Equation (2), with ϕ the phase shift that can be varied between $-\pi$ and π. Note that the power transfer of the DAB can be adjusted by controlling the variable phase shift.

$$P = \frac{n \cdot V_{out} V_{in} \phi (\pi - |\phi|)}{2\pi^2 f_s L} \quad (2)$$

This modulation can lead to high efficiencies, especially when the input and the primary side reflected output voltage levels are matched. A disadvantage of this modulation scheme is that circulating currents in the magnetic components can introduce significant losses for large values of ϕ [8]. Also, if the input and the reflected output voltage levels are not matched, the switching losses can increase significantly. This is particularly severe when zero voltage switching is lost, which is at the moment when either $\hat{I}_{L1}$ or $\hat{I}_{L2}$ are not large enough to charge and discharge the half-bridge parasitic capacitance or when they change polarity [9], [10]. The later condition can be translated into limitations on the power transferred, where Equation (3) and Equation (4) are the minimum requirements for achieving zero voltage switching.

$$\phi > \frac{\pi}{2} \left(1 - \frac{n \cdot V_{out}}{V_{in}} \right) \quad (3)$$

$$\phi > \frac{\pi}{2} \left(1 - \frac{V_{in}}{n \cdot V_{out}} \right) \quad (4)$$

90

These limits are visualized for different transformer turn ratios in Figure 4, where the area above the line indicates the region where zero voltage switching occurs. The inductance L and
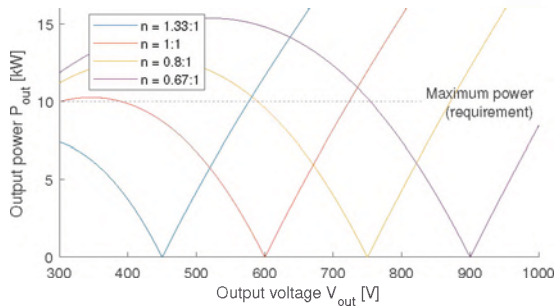

Fig. 4: Border for zero voltage switching in rectangular mode

switching frequency f_s are chosen in such a way that for all output voltages the rated power of $10\,\text{kW}$ is possible with a phase shift of $\pi/4$. The input voltage V_{in} is fixed at $600\,\text{V}$. As it can be observed, at matched voltage levels where the reflected output voltage equals the input voltage, the switching losses can be relatively low. However, if the voltage levels differ, especially under low power or partial load, zero voltage switching is not guaranteed and the switching losses could become expressively higher.

To overcome the shortcoming of a narrow region with low switching losses, a second modulation scheme is investigated, namely the triangular current modulation.

B. Triangular Current Modulation

Under triangular current modulation [7], the two equivalent voltage sources of Figure 2 are not limited to either the positive or the negative voltage, but a third level of $0\,\text{V}$ can be created on either side of the transformer. This enables the inductor current to have a triangular waveform, with a period of time when there is no current flowing through the transformer.

The first scenario of the triangular current modulation is when the input voltage V_{in} is larger than the reflected output voltage $n \cdot V_{out}$. The current and voltage waveform of this case is shown in Figure 5. The power transfer, as a function of the phase shift, is given by Equation (5).

$$P_{tri} = \frac{\phi^2 V_{in}(n \cdot V_{out})^2}{\pi^2 f_s L(V_{in} - n \cdot V_{out})} \quad (5)$$

From the waveform it becomes clear, that $T_1 + T_2 \leq T_s/2$. This has consequences for the maximum phase shift and hence the maximum amount of power that can be transferred. This upper limit is given in Equation (6).

$$P_{tri,max} = \frac{(V_{in} - n \cdot V_{out}) \cdot (n \cdot V_{out})^2}{4V_{in}f_s L} \quad (6)$$

The second scenario is when the reflected output voltage $n \cdot V_{out}$ is larger than the input voltage V_{in}. The waveform of this scenario is given in Figure 6, which is slightly different compared to the previous one. The power transfer is in this case given by Equation (7).

$$P_{tri} = \frac{\phi^2 n \cdot V_{out}V_{in}^2}{\pi^2 f_s L(n \cdot V_{out} - V_{in})} \quad (7)$$

With the same restriction as seen before ($T_1 + T_2 \leq T_s/2$), the maximum amount of power being transferred is given
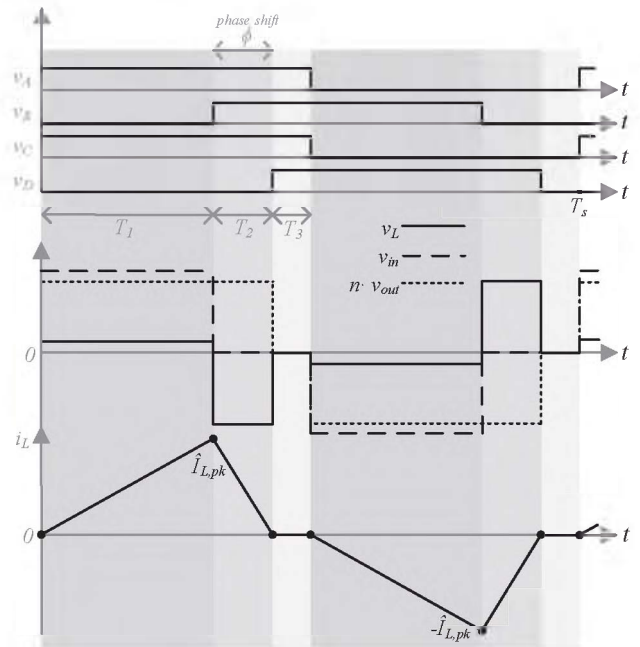

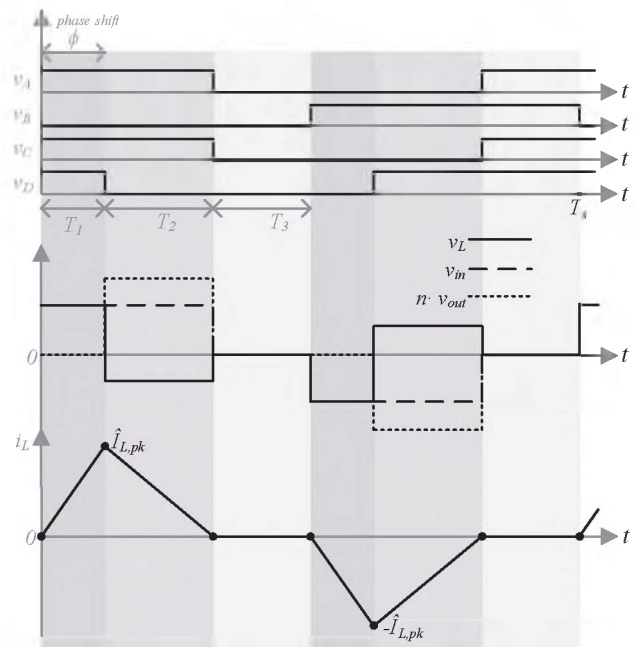Fig. 5: Triangular current modulation ($V_{in} > n \cdot V_{out}$)

Fig. 6: Triangular current modulation ($n \cdot V_{out} > V_{in}$)

91

by Equation (8).

$$P_{tri,max} = \frac{V_{in}^2(n \cdot V_{out} - V_{in})}{4n \cdot V_{out} f_s L} \qquad (8)$$

For triangular current modulation, two out of eight turn off switching transitions occur with a non-zero current. The other six turn off transitions and all eight turn on transitions occur at zero voltage and zero current [8]. A limitation of the triangular current modulation is the reduced maximum power transfer capability, which depends on the output voltage. Especially when the input and reflected output voltage are close to each other, only little to no power transfer is possible. Therefore, a third modulation method will be investigated, the trapezoidal current modulation in the following subsection.

C. Trapezoidal Current Modulation

The trapezoidal current modulation is similar to the triangular one with respect to the voltage levels that can be created on both sides. However, this time there is no moment included when there is no current flowing through the transformer. The waveforms of the current and voltage are given in Figure 7. In this figure the input voltage V_{in} is larger than the reflected output voltage $n \cdot V_{out}$. In case it is the other way around ($n \cdot V_{out} > V_{in}$), the first current peak $\hat{I}_{L,pk1}$ will be larger than the second $\hat{I}_{L,pk2}$. The power transfer is in each case given by Equation (9) [7].

$$P = \frac{n \cdot V_{out}}{4\pi^2 f_s L V_{in}} \cdot (4\phi^2(V_{in}n \cdot V_{out} - (V_{in} + n \cdot V_{out})^2) + 4\pi|\phi|(n \cdot V_{out})^2 + \pi^2(n \cdot V_{out}(V_{in} - n \cdot V_{out}))) \cdot \text{sign}(\phi) \qquad (9)$$

Given the shape of the current, this current modulation has not only a maximum power transfer at each different output
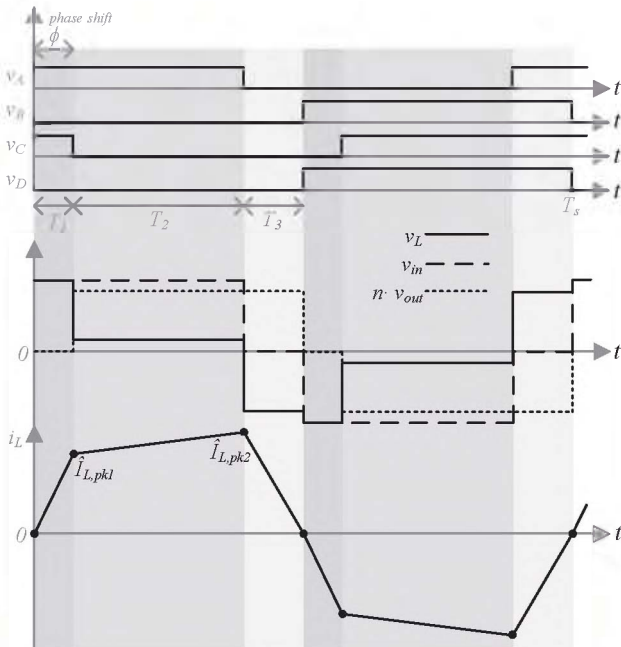

Fig. 7: Trapezoidal current modulation ($V_{in} > n \cdot V_{out}$)

voltage, but also a minimum. In the first case ($V_{in} > n \cdot V_{out}$) the minimum power transfer is given by Equation (10) and in the second case ($n \cdot V_{out} > V_{in}$) by Equation (11).

$$P_{trap,min} = \frac{(n \cdot V_{out})^2(V_{in} - n \cdot V_{out})}{4f_s L V_{in}} \qquad (10)$$

$$P_{trap,min} = \frac{V_{in}^2(n \cdot V_{out} - V_{in})}{4f_s L n \cdot V_{out}} \qquad (11)$$

It can be noticed that this is for each output voltage the same as the maximum power transfer in the triangular current modulation. Together, they can cover a wide output voltage and power range, shown in Figure 8. Switching between the triangular and trapezoidal current modulation schemes can be seamlessly, given that they both start from $i_L = 0\,\text{A}$ in each period. With respect to the switching losses of the trapezoidal current modulation, there are four out of eight turn off transitions happening at a finite amount of current, resulting in switching losses.
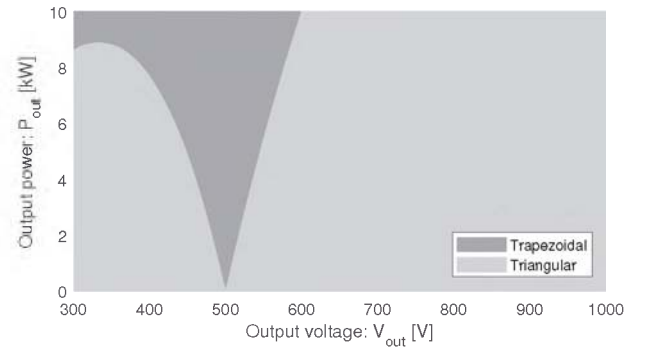

Fig. 8: Modulation schemes for the complete output voltage range ($n = 1.2$)

IV. DAB CONVERTER DESIGN

In order to design the DAB circuit components, the turns ratio of the transformer must be defined first. Then the commercial semiconductors will be chosen according to a suitable switching frequency operation and the highest current stresses, finally the passive components are designed.

A. Turns ratio

To find a proper turns ratio, an iterative algorithm is used to minimize the RMS and peak value of the current flowing in the transformer. This is chosen according to the steps described below:

1) Choose initial turns ratio;
2) Calculate RMS and peak value of the current in the complete output range (verify multiple operating points);
3) Determine a score of the chosen turns ratio based on the primary and secondary RMS and peak value of the current;
4) Increase or decrease the turns ratio and return to step 2.

If the score of the new turns ratio is lower than the previous one, the new turns ratio will increase or decrease again in

the same direction. If the score becomes higher, the turns ratio will increase or decrease in the other direction. If the searching direction has changed two times in a row, the step size is halved until a certain threshold. Then the best turns ratio has been found. The optimization process of the algorithm is shown in Figure 9, with the selected turns ratio of $n = 1.2$.
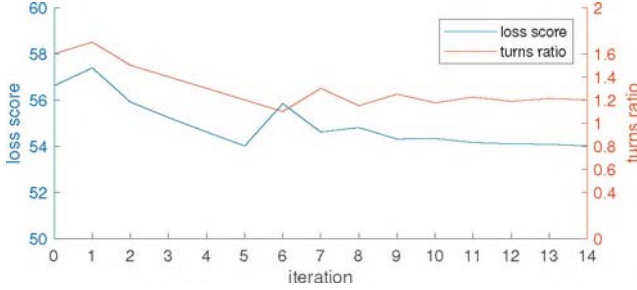

Fig. 9: Process of finding iteratively the best turns ratio $n = 1.2$ ($n_{init} = 1.6$)

B. Semiconductors

Suitable semiconductor technologies for the $10\,\text{kW}$ DAB are MOSFETs or IGBTs with anti-parallel diodes. For the rated power the current capability of the semiconductors should be at least $70\,\text{A}$. The calculated peak current with the chosen turns ratio was $66\,\text{A}$ on the secondary side. In order to compare both devices, an estimation is done for their losses. The conduction losses of a MOSFET can be estimated using Equation (12).

$$P_{MOSFET,cond.} = R_{DS,on} \cdot I_{RMS}^2 \qquad (12)$$

The influence of current on $R_{DS,on}$ can be neglected, but the influence of the junction temperature is considered. Using curve fitting a second order function has been derived to take this influence into account. Equation (13) shows the function for $R_{DS,on}$.

$$R_{DS,on} = 0.021 \times (2.10 \times 10^{-5} \cdot T_j^2 + 6.11 \times 10^{-4} \cdot T_j + 0.98) \qquad (13)$$

The conduction losses of an IGBT are calculated differently, considering also the influence of the bipolar forward voltage drop. The power loss is then described by Equation (14).

$$P_{IGBT,cond.} = R_{CE,on} \cdot I_{RMS}^2 + V_{CE,fw} \cdot I_{AVG} \qquad (14)$$

For conducting current in the opposite direction, the integrated anti-parallel diode is used. These conduction losses are given in Equation (15):

$$P_{IGBT,rev.cond.} = R_{D,on} \cdot I_{RMS}^2 + V_{D,fw} \cdot I_{AVG} \qquad (15)$$

The switches also suffer from switching losses. All turn on transitions were assumed lossless, so only the turn off transitions are taken into consideration. From the curves in the datasheets of both devices, equations are derived for the turn off losses based on the blocking voltage, the forward current through the device and the influence of the junction

temperature of the semiconductor. The power loss is then calculated as in Equation (16).

$$P_{turn-off} = (E_{off} - E_{oss}) \cdot f_s \qquad (16)$$

In Equation (16), E_{off} is the turn off energy loss, and E_{oss} is the stored energy in the parasitic output capacitance of the MOSFET (replace by E_{oes} for the IGBT) which helps reducing the turn off losses. An equation for this energy based on the voltage is derived from the related curves in the datasheet. Now the maximum switching frequency for both devices is investigated. Therefore, the maximum junction temperature is set to $135\,^{\circ}\text{C}$ and it is said the heat sink can hold a temperature of $100\,^{\circ}\text{C}$. Using the thermal resistance of the junction to case ($R_{\theta,j-c}$) found in the datasheet the maximum power loss can be found for a temperature increase that will not exceed the $135\,^{\circ}\text{C}$. It is found that the maximum switching frequency for a suitable SiC MOSFET is equal to $150\,\text{kHz}$, where a suitable Si IGBT can only withstand up to $18\,\text{kHz}$, which is considerably lower. If limits are applied for a preferable switching frequency, for example operation out of the audible range ($f_s > 16\,\text{kHz}$) and a switching frequency that can be simply controlled by a DSP and measured accurately by a conventional hall-effect current sensor ($f_s < 48\,\text{kHz}$), the MOSFET is the best option, particularly because the losses of the IGBT at $16\,\text{kHz}$ are much higher and difficult to manage. Thus, SiC MOSFETs are chosen. The switching frequency is not fixed yet, but a magnetic design will be done for three different frequencies first, namely $25\,\text{kHz}$, $35\,\text{kHz}$ and $45\,\text{kHz}$. The estimated losses of the magnetics and semiconductors are added in all three cases and the option with the lowest losses will determine the optimal switching frequency.

C. Magnetics

The design of the magnetics comprises the transformer and inductor. The transformer is the first one to be designed. For this, the procedures from [12] and [13] are followed. Starting by assembling the design inputs, which are given in Table I. Using the law of Faraday and understanding that the core

TABLE I: Assembling design inputs of the transformer

Parameter	Value
Rated primary voltage V_{pri}	$600\,\text{V}$
Rated RMS primary current I_{pri}	$35\,\text{A}$
Turns ratio n_{design}	1.2
Operating frequency f_s	$25\,\text{kHz}, 35\,\text{kHz}, 45\,\text{kHz}$
Maximum body temperature T_s	$100\,^{\circ}\text{C}$
Maximum ambient temperature T_a	$40\,^{\circ}\text{C}$

excitation is bidirectional one can write a relation between design parameters on one hand and core parameters on the other hand. This area product is given in Equation (17).

$$A_e A_w = \frac{V I_{pri}}{2 \hat{B} f_s k_w J} \qquad (17)$$

A selection is made from available cores and all their physical properties are put into an optimization routine. In

order to determine which core material should be used, the performance factor of the available core materials is compared, after which *N87* is chosen.

The number of primary turns is found by Equation (18) and the number of secondary turns can be found using the turns ratio.

$$N_{pri} = \frac{V_{in}}{4f_s A_e B_{rated}} \qquad (18)$$

Both solid and Litz wire technologies are investigated, where for Litz wire the diameter of a strand is chosen as 2δ, with δ being the skin depth at the given switching frequency. The Litz wire was chosen based on the lower estimated losses.

To limit the proximity effect losses, it is chosen to use a maximum of two layers for both the primary and secondary windings.

Furthermore, equations for the heat dissipation are used to determine the thermal resistance. Both radiative and convective heat transfer are taken into account, where the thermal resistance of each component is found by using the physical dimensions from the core database [12], combined with the estimated size of both coils. Note that both radiative and convective heat transfer are occurring at the same moment, so their thermal resistances can be placed in parallel.

With the core database created, all equations are added including the ones to determine the core and conduction losses for the specific design and the resulting rise in temperature. This enables the possibility to change parameters in the design, with each change immediately mapped to a different value of power loss, volume and maximum temperature. In this way the magnetic design could be optimized for the smallest size or the minimum power loss. For the design of the 25 kHz transformer, two *TDK UI126/119/20* cores are combined to form an E-core, with the number of primary and secondary turns equal to 26 and 22 respectively.

With the transformer design completed, the leakage inductance can be calculated and based on the required inductance an auxiliary inductor can be designed using a similar approach as for the transformer. The design inputs are given in Table II and in order to choose a core, a relation is again found between design and the core parameters, shown in Equation (19).

TABLE II: Assembling design inputs of the inductor

Parameter	Value
Rated voltage V_{in}	600 V
Rated RMS current I_{rms}	35 A
Rated peak current $\hat{I}$	55 A
fsL-product $f_s L$	1.503 Hz − H
Operating frequency f_s	25 kHz, 35 kHz, 45 kHz
Maximum body temperature T_s	100 °C
Maximum ambient temperature T_a	40 °C

$$A_w A_e = \frac{L I_{rms} \hat{I}}{k_w J_{rms} \hat{B}} \qquad (19)$$

The number of turns that will fit in the core window is then found by Equation (20). For the inductor and transformer the same type of wire will be used.

$$N = \left\lfloor \frac{k_w A_w}{A_{Cu}} \right\rfloor \qquad (20)$$

By adjusting the length of the air gap the correct inductance can be set, see Equation (21).

$$l_g = \frac{\mu_0 N \hat{I}}{N_g \hat{B}} \qquad (21)$$

Using the same optimization procedure as for the transformer, the inductor operating at 25 kHz uses an *TDK E70/33/32* core with 13 turns and an air gap of 2.14 mm.

The process is repeated for the other two selected switching frequencies. Then, the losses of both the semiconductors and magnetics are compared at the three different operating frequencies. The semiconductor losses include both conduction and switching and the losses of the magnetics consists of core and winding losses. For the power transfer of 10 kW, the estimated losses are depicted in Figure 10.

If the average losses are compared, there is no significant difference. At partial load of 2 kW and 6 kW the same tendency is observed. However, the design of 35 kHz has a negligible higher loss. The main difference is found on how the losses are spread across the magnetics and semiconductors. In the followings, the switching frequency of 25 kHz is selected for the prototype because it constitutes a conservative approach in case the semiconductor models derived from the data-sheet are not accurate enough.

The next step is the design of the capacitors.

D. Capacitors

Based on the maximum allowed output voltage ripple the capacitors will be chosen. For each operating mode equations are derived to calculate the accumulated charge. A script is coded to evaluate the maximum required charge in the complete output range, then a minimum capacitance is found by setting the maximum allowed output ripple. For this design and a maximum voltage ripple of 10 V, a capacitor of about 29.3 μF is required. Film capacitors are chosen [14] and two capacitors of 20 μF are placed in parallel. Deriving equations for the RMS currents in and out of the capacitors leads to an estimation of the losses due to the equivalent series resistance.

E. Heatsink

Based on the maximum losses a heatsink is chosen, able to keep the junction temperature of each MOSFET below the maximum allowed 135 °C. Taking into account that the losses can be slightly higher (20 %) and the temperature in the converter box can be 10 °C higher than the ambient, a heat sink with a thermal resistance of 0.40 °C W^{-1} is required. Therefore a miniature cooling aggregate from Fischer Elektronic is used, consisting of two fans which will consume roughly an additional 2.5 W.
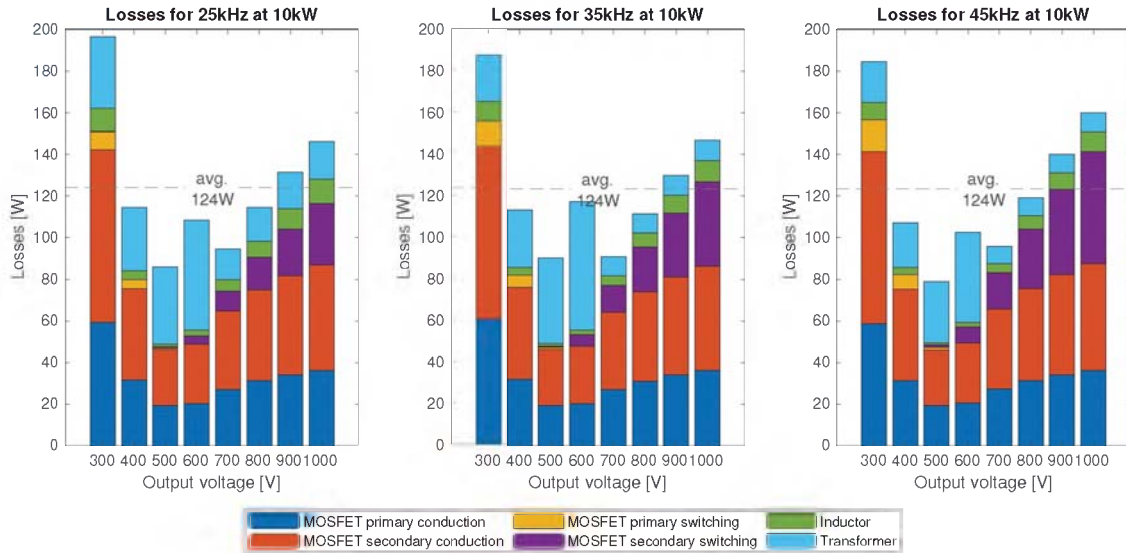
94

Fig. 10: Comparison of the losses in both the semiconductors and magnetics for three different designs

F. Control circuit

A Texas Instruments launchpad is used for controlling the converter.

G. 3D Drawing of the DAB Prototype

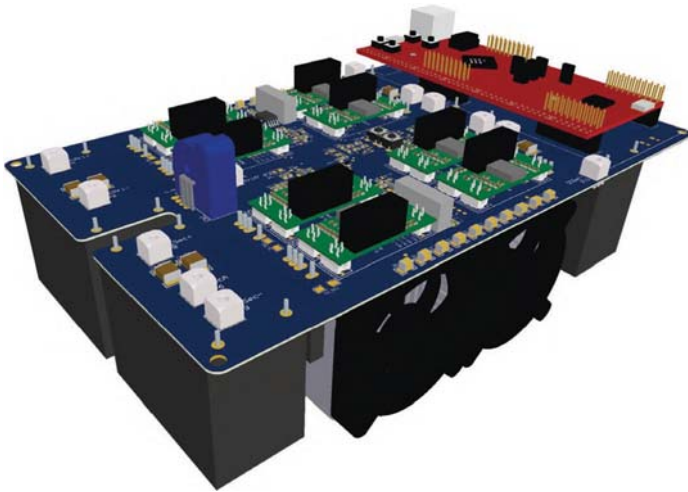A 3D drawing of the designed DAB is shown in Figure 11.

Fig. 11: 3D drawing of the designed DAB prototype. Note that the magnetics are not shown but they should be accommodated underneath the circuit

V. CALCULATED EFFICIENCY

A. Overall efficiency

For the complete range from an output power of $1\,\mathrm{kW}$ up to $10\,\mathrm{kW}$ and an output voltage of $300\,\mathrm{V}$ up to $1000\,\mathrm{V}$, the efficiency is determined. For this calculation, the losses of the semiconductors (conduction and switching), magnetics
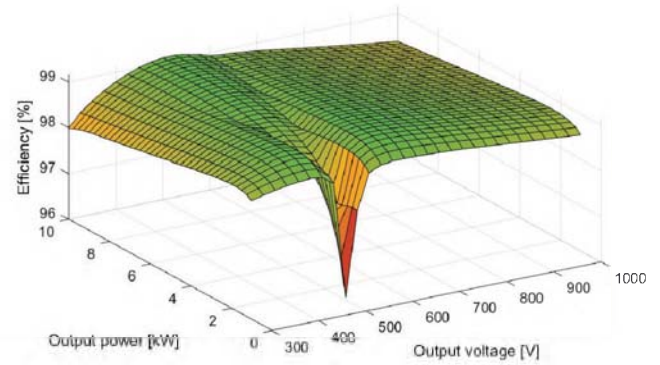

Fig. 12: Overall efficiency of the $10\,\mathrm{kW}$ DAB converter in tri- angular and trapezoidal operating mode according to Figure 8

(winding and core), capacitors (equivalent series resistance and resistive discharge) and the losses of the fans are taken into account. Furthermore, for the control circuitry an ad- ditional $5\,\mathrm{W}$ of power loss is used. An overview with the most important components is given in Table III. The overall

TABLE III: List of the DAB components

Component	Type
MOSFET	Cree C3M0021120K
Output capacitor	2 KEMET C4AQUBW5200A3MJ
Core transformer	2 TDK UI126/119/20
Core inductor	TDK E70/33/32
Heat Sink	Fischer Elektronic LAM 5 D K 125 12
Development board	Texas Instruments F28379D

efficiency is given in Figure 12. The average efficiency is $98.9\,\%$, with a maximum efficiency $99.2\,\%$. In the region

95

where the input voltage equals the reflected output voltage ($V_{in} = n \cdot V_{out}$) and trapezoidal current modulation is applied, the largest differences are seen in efficiency with respect to a changing power, which is due to the relatively large losses in the transformer core. At low partial load, in the trapezoidal modulation the small phase-shift angle will lead to a relatively high magnetic flux density in the cores when compared to the triangular modulation.

B. Simulation charging profile

Next, the charging profile for the battery of an electric vehicle is used, to check the performance of the converter in a use case. The charging profile is given in Figure 13. The average efficiency of the complete simulated charging process is 98.8 %.
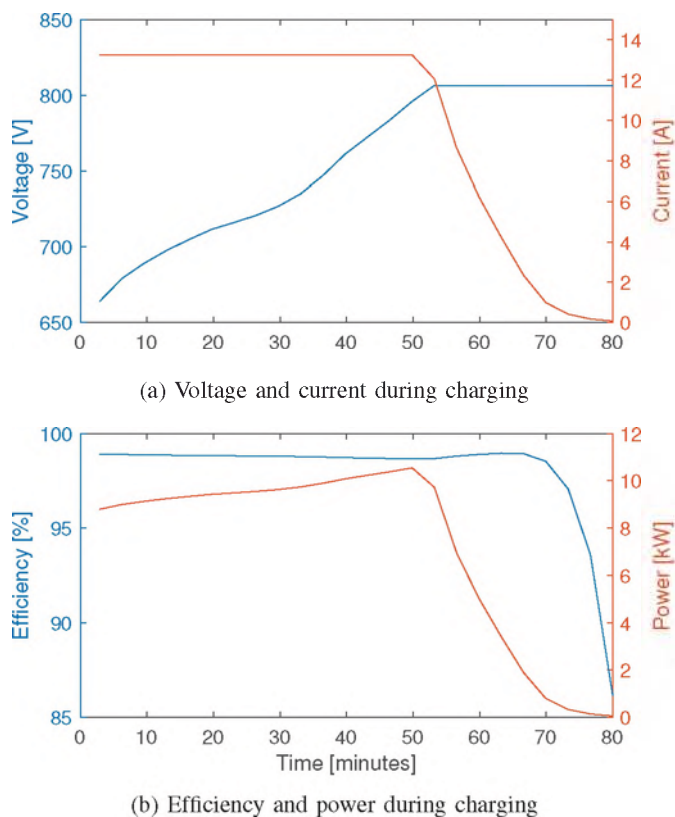

(a) Voltage and current during charging

(b) Efficiency and power during charging

Fig. 13: The charging and power profile of the simulated battery of an electrical vehicle

VI. CONCLUSIONS

The topology of the dual active bridge converter seems a good candidate for the charging of electrical vehicles. Firstly, the rectangular current modulation was discussed, but the expectation was that the losses in the wide output voltage range would be unsatisfactory. Then, both the triangular and trapezoidal current modulation techniques were investigated and chosen as promising modulation schemes. For the semi-conductor Si IGBT and SiC MOSFET were compared in terms of losses, where it was concluded the MOSFET would perform best in the given charger specifications. Magnetic components were designed and a switching frequency of 25 kHz was chosen to the final design. The efficiency of the converter was evaluated in the complete operating region, where an average efficiency of 98.9 % was found. For a typical use case the overall efficiency during the charging process of a car battery was also simulated, with a resulting average efficiency of 98.8 %. All in all the results show that the DAB circuit is a promising candidate for the charging of electric vehicles.

VII. FUTURE WORK

In order to verify the performance of the design, the converter will be build and tested. The efficiency will be measured and it should become clear if the modelling of the losses was accurate enough.

REFERENCES

[1] F. Marra, G. Y. Yang, C. Træholt, E. Larsen, C. N. Rasmussen, and S. You, "Demand profile study of battery electric vehicle under different charging options," 2012 IEEE Power and Energy Society General Meeting, pages 1–7, 2012.

[2] T. B. Soeiro and P. Bauer, "Fast DC-Type Electric Vehicle Charger Based On A Quasi-Direct Boost - Buck Rectifier," 2019 AEIT International Conference of Electrical and Electronic Technologies for Automotive (AEIT AUTOMOTIVE), Torino, Italy, 2019, pp. 1-6.

[3] T. B. Soeiro, M. Ortmann and M. L. Heldwein, "Three-phase fivelevel bidirectional buck- + boosttype PFC converter for DC distribution systems," 2013 IEEE International Conference on Industrial Technology (ICIT), Cape Town, 2013, pp. 928-933.

[4] T. B. Soeiro, M. L. Heldwein and J. W. Kolar, "Three-phase modular multilevel current source rectifiers for electric vehicle battery charging systems," in Proc. of Brazilian Power Electronics Conference (COBEP), 2013.

[5] S. A. Gorji, H. G. Sahebi, M. Ektesabi, and A. B. Rad, "Topologies and control schemes of bidirectional dc–dc power converters: An overview," IEEE Access, 7:117997–118019, 2019.

[6] B. Zhao, Q. Song, W. Liu, and Y. Sun, "Overview of dual-active-bridge isolated bidirectional dc–dc converter for high-frequency-link power-conversion system," IEEE Transactions on Power Electronics, 29(8):4091–4106, Aug 2014.

[7] F. Krismer, "Modeling and Optimization of Bidirectional Dual Active Bridge DC–DC Converter Topologies," PhD thesis, ETH Zürich, 2010.

[8] Y. Wang, "Thermal Management of High-Current Bidirectional Isolated DC-DC Converters," PhD thesis, Delft University of Technology, 2015.

[9] V. M. Iyer, S. Gulur, and S. Bhattacharya, "Optimal design methodology for dual active bridge converter under wide voltage variation," 2017 IEEE Transportation Electrification Conference and Expo (ITEC), pages 413–420, June 2017.

[10] H. Ramakrishnan, "Design guide: Tida-010054 - bi-directional, dual active bridge reference design for level 3 electric vehicle charging stations," Texas Instruments Incorporated, June 2019.

[11] F. Grazian, P. van Duijsen, T. B. Soeiro and P. Bauer, "Advantages and Tuning of Zero Voltage Switching in a Wireless Power Transfer System," 2019 IEEE PELS Workshop on Emerging Technologies: Wireless Power Transfer (WoW), London, United Kingdom, 2019, pp. 367-372.

[12] N. Mohan, T.M. Undeland, and W.P. Robbins, "Power Electronics: Converters, Applications and Design," Wiley, third edition, 2003.

[13] P. S. Kumar, "Design of high frequency power transformer for switched mode power supplies," 2016 International Conference on Emerging Trends in Engineering, Technology and Science (ICETETS), pages 1–5, 2016.

[14] H. Wang, "Iecon 2016 tutorial: Capacitors in power electronics applications – reliability and circuit design," https://vbn.aau.dk/ws/portalfiles/portal/243654015/IECON_2016_Cap_HW.pdf, 2016.